Control of magnetoelectric coupling in the Co₂Y-type hexaferrites

Chang Bae Park,[1] Kwang Woo Shin,[1] Sae Hwan Chun,[1] Jun Han Lee,[3] Yoon Seok Oh,[3] Steven M. Disseler,[4] Colin A. Heikes,[4] William D. Ratcliff,[4] Woo-Suk Noh,[5] Jae-Hoon Park,[5,6] and Kee Hoon Kim[1,2,*]

[1]*Center for Novel States of Complex Materials Research, Department of Physics and Astronomy,*
Seoul National University, Seoul 08826, South Korea

[2]*Institute of Applied Physics, Department of Physics and Astronomy, Seoul National University, Seoul 08826, South Korea*

[3]*Department of Physics, Ulsan National Institute of Science and Technology, Ulsan 44919, Republic of Korea*

[4]*NIST Center for Neutron Research, National Institute of Standards and Technology, Gaithersburg, Maryland 20899, USA*

[5]*Max Planck POSTECH Center for Complex Phase Materials, Pohang University of Science and Technology,*
Pohang 790-784, Republic of Korea

[6]*Department of Physics and Division of Advanced Materials Science, Pohang University of Science and Technology,*
Pohang 790-784, Republic of Korea

We comprehensively investigated the magnetic, ferroelectric, and ME properties of $Ba_{2-x}Sr_xCo_2(Fe_{1-y}Al_y)_{12}O_{22}$ single crystals in broad doping ranges of Sr ($1.0 \leqslant x \leqslant 1.8$) and Al ($0.00 \leqslant y \leqslant 0.08$). Most of the investigated compounds exhibit an intriguing coexistence of two apparently competing magnetic phases: a transverse conical (TC) and alternating longitudinal conical (ALC) spin structure. The magnetic properties show that the $Ba_{0.2}Sr_{1.8}Co_2(Fe_{0.96}Al_{0.04})_{12}O_{22}$ crystal has the highest ordering temperature and largest volume fraction of the ALC phase at zero H; further, after the application of an in-plane H, it exhibits a maximized volume fraction of the metastable TC phase, resulting in the highest ME susceptibility and electric polarization at all temperatures below 300 K. Our findings demonstrate that securing the thermal stability of the ALC phase is a crucial prerequisite to achieve optimized ME coupling in Co₂Y-type hexaferrites, pointing to a general strategy applicable to other hexaferrites as well.

I. INTRODUCTION

For more than a decade, multiferroic or magnetoelectric (ME) materials, in which magnetic and ferroelectric orders coexist and are strongly coupled to each other, have been studied extensively. Both their scientific novelty in relation to the mechanism of strong ME coupling [1–4] and their potential for realizing multifunctional electronic devices [5] have been major driving forces for the extensive worldwide research activity on these materials. Although various new mechanisms and emergent materials have been discovered [1,2,4,6,7], multiferroic or ME materials with strong ME coupling at room temperature are still rare. Only a limited number of materials such as $BiFeO_3$ and Cr_2O_3 have been known to exhibit sizable ME coupling at room temperature [8,9]. However, the ME coupling strength of those compounds is yet small for practical applications; for example, the ME susceptibility, defined here as the derivative of electric polarization (P) with respect to the applied magnetic field (H), dP/dH, shows a maximum of ∼3 ps/m for Cr_2O_3 [8] and ∼55 ps/m for $BiFeO_3$ [9] at 300 K. Therefore, the exploration of new multiferroics that can exhibit higher ME coupling strengths at room temperature is of high research interest.

In order to achieve strong ME coupling near room temperature, several ferrites with various hexagonal crystal structures

(e.g., Z-, Y-, U-, and W- types) have been studied [10]. In these hexaferrites, the geometric frustration at the interface of the two neighboring magnetic blocks often results in noncollinear spin structures such as conical spin order [see also, Fig. 1(a)], which are key to the generation of spin-driven ferroelectricity via the inverse Dzyaloshiskii-Moriya mechanism [6,11–13]. More importantly, these hexaferrites exhibit several intrinsic material properties that can allow strong ME coupling near room temperature [12,14–17]. First, the conical spin ordering in several hexaferrites occurs at above room temperature. For example, the transverse conical (TC) ordering temperature T_{con} of the Co₂Z-type hexaferrite $Ba_{0.52}Sr_{2.48}Co_2Fe_{24}O_{41}$ is 413 K [12], allowing the room-temperature operation of ME effects. Second, the critical magnetic field for P switching is mostly quite low [18–21], presumably because of the soft nature of the conical spin structure. Consequently, the direction of electric polarization can be easily reversed at a very small H bias of ∼1 mT, as demonstrated in the Zn₂Y-type hexaferrite $Ba_{0.5}Sr_{1.5}Zn_2(Fe_{0.92}Al_{0.08})_{12}O_{22}$ [6]. Third, magnetization reversal through the application of an electric field without H bias has been demonstrated in the Y-type hexaferrites ($\pm 2\,\mu_B$/f.u. under ± 2 MV/m); magnetic softness and giant direct ME coupling were key material properties that lead to such giant converse ME effects [11].

Owing to these multiple advantages, Y-type hexaferrites are drawing much research attention [22–24]; they offer great potential for realizing the electric field (E) control of

---
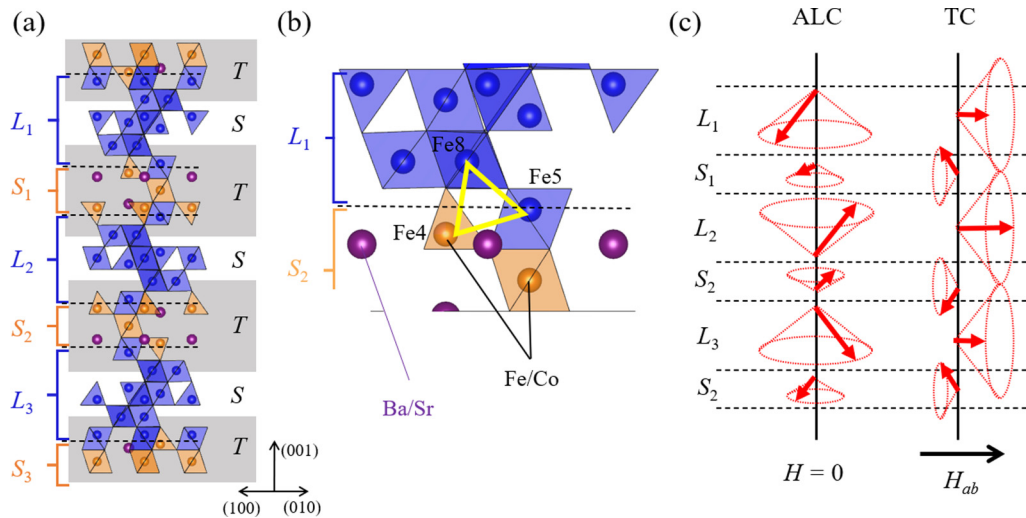
*Corresponding author: khkim@phya.snu.ac.kr

FIG. 1. (a) The crystal structure of Co_2Y-type hexaferrites and (b) a magnified view of the structure around the interface of the magnetic blocks. Both Fe and Co ions can occupy the center of the oxygen octahedra or tetrahedra. Orange and blue colors represent Fe or Co ions in the magnetic L and S blocks, respectively, while purple spheres represent Ba or Sr sites. The yellow triangle indicates the spin network with geometrical spin frustration related to helical spin ordering in the Co_2Y-type hexaferrites. (c) Schematic representation of the spin configuration of the Co_2Y-type hexaferrites without (left) and with (right) the application of an in-plane magnetic field (H_{ab}). ALC refers to an alternating conical spin ordering pattern, and TC represents a transverse conical spin ordering pattern.

magnetization (M) reversal at room temperature owing to their large direct ME coupling, which results in a sharp increase (decrease) of P at a small positive (negative) H bias. On the other hand, the T_{con} of most Y-type hexaferrites is below room temperature, hindering the realization of ME effects near room temperature. It has been reported that T_{con} can be increased when zinc ions are replaced by cobalt ions in ceramic samples [24]. However, it is difficult to quantify intrinsic ME effects in ceramic samples because of the trapped charges in their grain boundaries. Figure S1 [25] illustrates that the ME properties of ceramic and single-crystal samples do not coincide at the same nominal composition [14,26], suggesting that a systematic study in a single-crystal form is required to understand the intrinsic ME coupling in Co_2Y-type and related hexaferrites. Along these lines, Kocsis *et al.* recently showed that a $Ba_{0.8}Sr_{1.2}Co_2Fe_{11.1}Al_{0.9}O_{22}$ single crystal having a high resistivity due to oxygen annealing can induce M reversal through E control at room temperature [22]. On the other hand, although numerous attempts have been made to increase the ME coupling via, e.g., chemical substitution and structural modifications, it is still unknown how the ME coupling can be maximized in these hexaferrites with regards to the variation of intrinsic material properties such as magnetic anisotropy and spin ordering temperatures.

In this study, we systematically explore the physical properties of $Ba_{2-x}Sr_xCo_2(Fe_{1-y}Al_y)_{12}O_{22}$ (BSCFAO) single crystals to find the optimal ME coupling strength near room temperature. We extensively investigate magnetic, electric, and ME properties of single crystals of BSCFAO with various doping ratios x and y. The specimen with $x = 1.8$ and $y = 0.04$ exhibits the largest ME susceptibility values at temperatures between 10 and 300 K ($\sim$25 000 ps/m at 10 K and $\sim$1000 ps/m at 300 K). Moreover, systematic studies of the magnetic and electrical phase diagram reveal that the volume fraction of TC and thermal stability of the alternating longitu-

dinal conical (ALC) phase, representing the high free-energy barrier between the ALC and TC phases, are linked to each other and are key to achieving the strongest ME coupling in these Co_2Y-type hexaferrites at room temperature as well as low temperatures. In particular, the stabilization of the ALC phase without net magnetic moment along the c axis, not the normal longitudinal conical phase (NLC) with finite magnetic moment along the c axis [27], is emphasized to be important for stabilizing the TC phase under magnetic fields; the strong uniaxial spin anisotropy preferring the staggering along the c axis in the ALC phase at zero magnetic field simultaneously makes the TC phase represented by ab-plane spin anisotropy become more stable under magnetic fields. Based on this mechanism, we could achieve an optimization of ME coupling in $Ba_{0.2}Sr_{1.8}Co_2(Fe_{0.96}Al_{0.04})_{12}O_{22}$ through the tuning of the strong magnetic anisotropy via chemical doping.

II. CRYSTAL STRUCTURE AND XRD ANALYSIS

Hexaferrites are composed of combinations of three crystallographic blocks: rhombohedral (R), spinel (S), and tetragonal (T) blocks [28,29]. In particular, one hexagonal unit cell of a Y-type hexaferrite contains only S and T blocks, as shown in Fig. 1(a). The T block is placed at the bottom of the unit cell, and the S block is stacked on top of the T block. A T' block (the $'$ symbol indicates $120°$ rotation along the c axis) and an S'' block are stacked on the first two blocks. Finally, S'' and T'' blocks are stacked to complete the unit cell of the Y-type hexaferrite. The spin structure of the Y-type hexaferrite can be divided into two major spin moment blocks, large (L) and small (S), as shown in Fig. 1(c). The chemical substitutions in the octahedral and tetrahedral sites of Fe/Co result in the variation of magnetic anisotropy within the L and S blocks, enabling the control of ME coupling.

Crystallographic structures of our $Ba_{2-x}Sr_xCo_2(Fe_{1-y}Al_y)_{12}O_{22}$ single crystals have been confirmed by powder x-ray diffraction and the Rietveld refinement. Figure S2(a) shows an x-ray diffraction pattern of a ground powder of a $Ba_{0.2}Sr_{1.8}Co_2Fe_{12}O_{22}$ single crystal and a refined curve by the Rietveld method, confirming that the Y-type hexaferrite shown in Fig. 1(a) is successfully grown [25]. We have also performed similar analyses on the other composition of $Ba_{2-x}Sr_xCo_2(Fe_{1-y}Al_y)_{12}O_{22}$ single crystals. The x-ray data analyses have ensured that all the single crystals investigated have Bragg peaks consistent with the Y-type hexaferrite structure with the $R\bar{3}m$ space group [17,29]. Moreover, it is clearly found that the lattice constants (a and c) of $Ba_{2-x}Sr_xCo_2(Fe_{1-y}Al_y)_{12}O_{22}$ obtained from the refinement decrease almost linearly in proportion to Sr (x) and Al (y) doping ratios [Fig. S2(b)] [25]. In both Y- and Z-type hexaferrites [12,30], it has been known that Sr substitution for Ba tends to reduce c and a values, which in turn seem to be useful to stabilize noncollinear spin states such as a helical phase and a TC phase, respectively. The results in Fig. S2(b) indicate that not only Sr but also Al substitution plays a role to reduce the c and a values further [25]. Thus, simultaneous substitution of both Sr and Al might constitute an effective route to stabilize the noncollinear spin orderings and to enable the study of unprecedented phase diagram in $Ba_{2-x}Sr_xCo_2(Fe_{1-y}Al_y)_{12}O_{22}$.

III. EFFECT OF THE TWO PHASE COEXISTENCE ON THE MAGNETIC AND ELECTRICAL PROPERTIES

Figure 2 presents Sr- and Al-doping effects on the H-induced electric polarization P and related ME susceptibility dP/dH for single crystals of $Ba_{2-x}Sr_xCo_2(Fe_{1-y}Al_y)_{12}O_{22}$. All the P data were obtained from the integration of ME current data at various temperatures between 10 and 300 K. Figure 2(a) shows the P//[120] variation with respect to H // [100] measured with either increasing or decreasing H after the ME poling at $\mu_0H = 0.1$ T. At 10 K, the $P–H$ curve typically exhibits a sharp increase (decrease) of P at a small positive (negative) H bias, resulting in a very asymmetric line shape in which the sign of P changes with the reversal of the H direction. This is a characteristic $P–H$ curve that has also been realized in the archetypal Y-type hexaferrite $Ba_{0.5}Sr_{1.5}Zn_2(Fe_{0.92}Al_{0.08})_{12}O_{22}$ at 10 K [6,11].

The asymmetric line shape of the $P–H$ curve is closely associated with the field-induced stabilization of the TC phase. Several neutron diffraction studies on $Ba_{0.5}Sr_{1.5}Zn_2(Fe_{0.92}Al_{0.08})_{12}O_{22}$, $Ba_{0.3}Sr_{1.7}Co_2Fe_{12}O_{22}$, and similar Y-type hexaferrites at broad Sr doping regions ($\sim0.8 < x < \sim1.8$) have demonstrated that a dominant phase at zero field below ~300 K is the ALC phase [15,16,18,31,32]. Moreover, by applying in-plane H, the ALC phase is suppressed and TC phase becomes stabilized at H above ~1 T. Once the TC phase is stabilized, it remains robust without changing to the ALC phase even after turning off the field; thus, it is called a "metastable" phase. This implies that, on decreasing the field, a TC phase stabilized once at a high field is subject to only in-plane spin rotation at lower fields because the magnetic easy axis of the TC phase is in the ab plane.
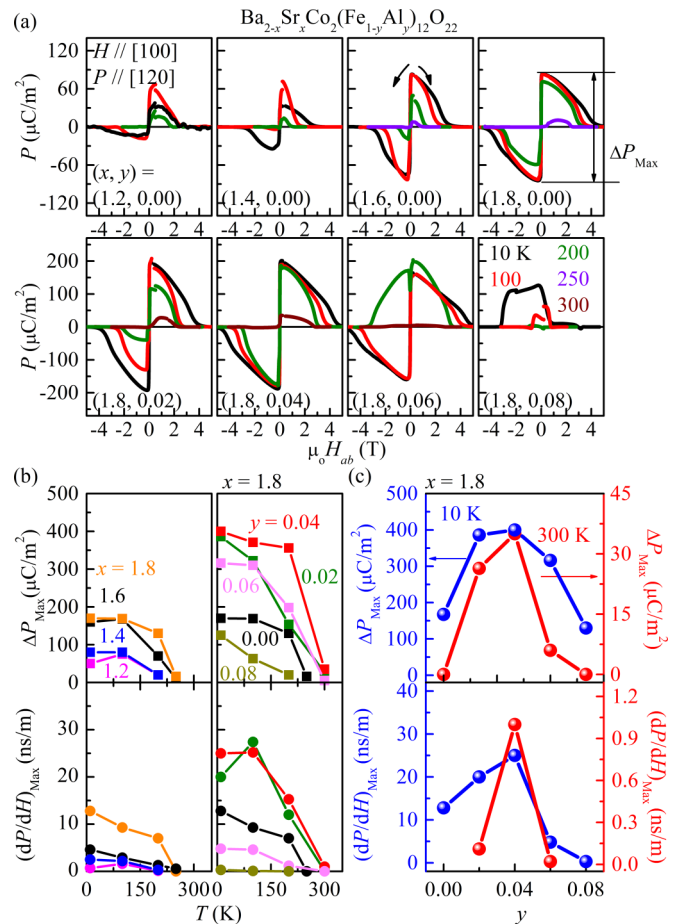

FIG. 2. (a) Field-induced electric polarization behavior of $Ba_{2-x}Sr_xCo_2(Fe_{1-y}Al_y)_{12}O_{22}$ single crystals under the application of in-plane magnetic fields (H_{ab}, H//[100]). ΔP_{Max} indicates the difference between extreme values, $P_{Max} - P_{Min}$. Electric polarization is calculated through the integration of the ME current. (b) Temperature dependence of ΔP_{Max} and maximum dP/dH values. (c) Summary of ΔP_{Max} and maximum dP/dH as a function of y at 10 and 300 K, demonstrating that the specimen with $x = 1.8$ and $y = 0.04$ has the highest magnetic-field-induced polarization and ME susceptibility at both temperatures.

However, as the temperature is increased, the asymmetric line shape of the $P–H$ curve becomes increasingly symmetric. At 300 K, most $P–H$ curves exhibit a positive P at a positive H bias. On performing ME poling at $\mu_0H = -0.1$ T, P continues to exhibit a positive value, even at negative H bias, resulting in a nearly symmetric $P–H$ curve (not shown (Note that the nearly zero P at a negative H bias in Fig. 2(a) is due to the lack of proper poling at the negative H region in the H-sweep process.) This observation at high temperatures of ~300 K implies that the spin rotation axis of the TC phase is increasingly subject to rotation via the c axis in the decreasing-field sweep, resulting in the stabilization of the ALC phase at low fields [33] (see, Fig. 1(c) for spin patterns). Therefore, it is likely that the metastable TC phase realized after turning off the field mostly remains stable at low temperatures, while the ALC phase becomes increasingly stabilized at high temperatures and coexists with the TC phase.
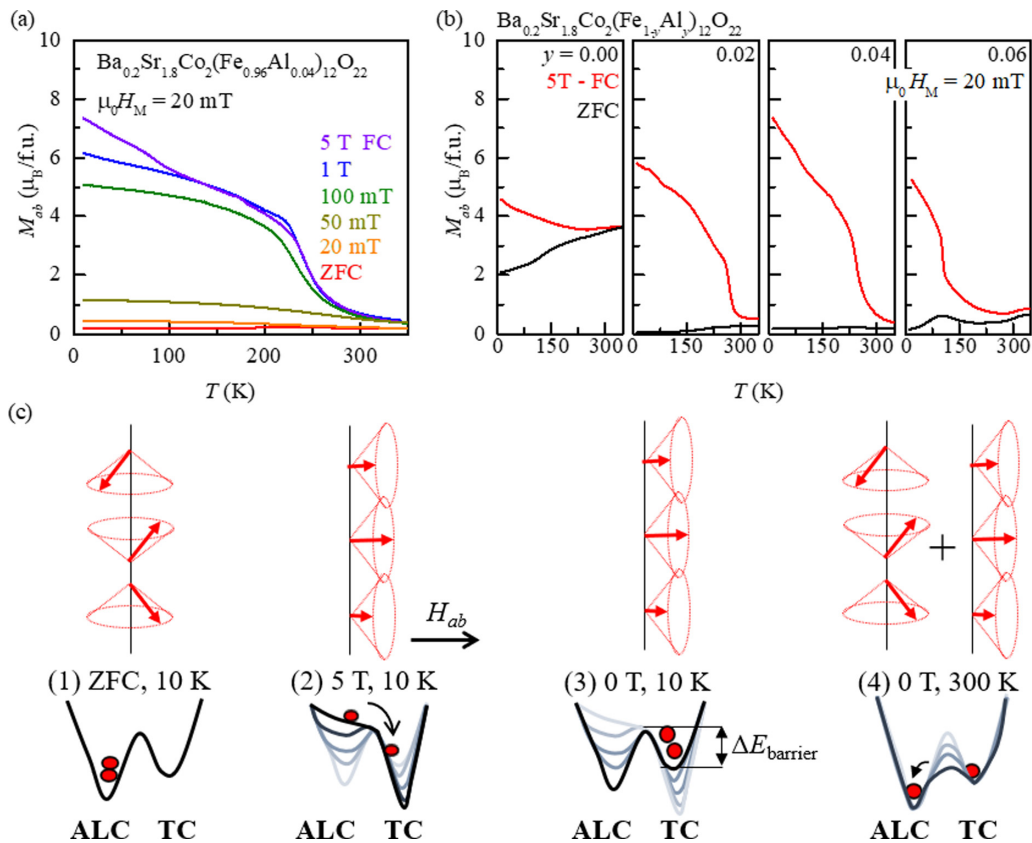
FIG. 3. (a) In-plane magnetization M_{ab} of $Ba_{0.2}Sr_{1.8}Co_2(Fe_{0.96}Al_{0.04})_{12}O_{22}$ from 10 to 350 K measured at a bias magnetic field $\mu_0H_M = 20$ mT after field cooling (FC) at various magnetic fields, demonstrating the metastable nature of the TC phase. (b) The red and black curves represent the M_{ab} of $Ba_{0.2}Sr_{1.8}Co_2(Fe_{1-y}Al_y)_{12}O_{22}$ measured under $\mu_0H_M = 20$ mT during the warming process after FC at 5 T (5T-FC) and zero-field cooling (ZFC), respectively. (c) Upper and lower panels schematically show dominant spin configurations (ALC or TC) and the corresponding free-energy landscape, respectively, when the system is subject to different temperature and magnetic-field conditions sequentially from (1) to (4): (1) ZFC at 10 K, (2) the application of $\mu_0H = 5$ T at 10 K, (3) turning off the field to 0 T at 10 K, and finally (4) increasing the temperature up to 300 K at 0 T. The black (most white gray) curve represents the schematic free-energy landscape at each step (the previous step). The brightness from white to black indicates the intermediate free-energy landscapes upon the variation of the magnetic field or temperature. Note that to represent the ALC or TC phase, we only draw the L block for simplicity.

The volume fraction or stability of the TC phase can be proportional to the remanent magnetization after field cooling (FC) because the TC phase essentially exhibits a large magnetic moment. On the other hand, the ALC phase, which has an antiferromagnetic spin configuration, exhibits quite a small magnetic moment. In order to check whether the metastable nature of the TC phase persists in the $Ba_{0.2}Sr_{1.8}Co_2(Fe_{1-y}Al_y)_{12}O_{22}$ series, we have studied the temperature-dependent in-plane magnetic moment M_{ab} at a small bias field of 20 mT (warming) after applying various FC processes. A result for $Ba_{0.2}Sr_{1.8}Co_2(Fe_{0.98}Al_{0.04})_{12}O_{22}$ is summarized in Fig. 3(a). The M_{ab} curves measured after zero-field cooling (ZFC) or FC at 20 and 50 mT remain mostly small (less than $0.5\,\mu_B$/f.u.) at all temperatures below 350 K, indicating that the ALC phase is predominantly stabilized by zero-field cooling (ZFC) or FC below 100 mT. On the other hand, the FC curves measured above 100 mT show rapid increase at temperatures below $\sim$250 K, and their M_{ab} values below 250 K become larger than $4\,\mu_B$/f.u and stay nearly high between 4 and $\sim$7 μ_B/f.u. This observation suggests that FC above 100 mT is sufficient to make the TC phase metastable and the TC phase remain stable dom-

inantly below $\sim$250 K. We find that all members of the $Ba_{0.2}Sr_{1.8}Co_2(Fe_{1-y}Al_y)_{12}O_{22}$ series studied here have such a metastable nature reflected in the M_{ab} curves measured after ZFC or various FC processes (see Fig. S3) [25]. It is noteworthy in Fig. 3(b) that the M_{ab} curves after FC at 5 T and ZFC are most substantially different in the $y = 0.04$ compound of the $Ba_{0.2}Sr_{1.8}Co_2(Fe_{1-y}Al_y)_{12}O_{22}$ series. Moreover, the temperature at which the curve for FC at 5 T starts to increase is the highest. Therefore, it is concluded that both the volume fraction and temperature stability of the TC phase remaining after FC are optimized in the $y = 0.04$ compound.

The metastable nature of the TC phase realized in a broad doping range of $Ba_{0.2}Sr_{1.8}Co_2(Fe_{1-y}Al_y)_{12}O_{22}$ can be qualitatively understood from the sequential evolution of schematically drawn free-energy landscape in Fig. 3(c) [15,31]. Upon being cooled down at zero field [(1) ZFC], the system is predominantly in the ALC phase, the stability of which is expected to depend on the spin frustration as well as magnetic anisotropy. As soon as a field up to 5 T is applied at low temperatures, the phase changes to the TC phase that forms the minimum free-energy under the magnetic field [(2) 5 T, 10 K]. Upon turning off the field, the system

remains in the TC phase at 10 K because the barrier height $\Delta E_{\text{barrier}}$ between the TC and ALC phase is high enough to prevent the phase transformation at low temperatures [(3) 0 T, 10 K]. When temperature is increased again, the system can populate both the ALC and TC phases by thermal excitation, and the volume fraction of each phase depends on the $\Delta E_{\text{barrier}}$ between the two phases [(4) 0 T, 300 K]. Accordingly, the $y = 0.04$ compound is expected to have the sharpest and deepest potential shape in the TC phase to have the largest value of $\Delta E_{\text{barrier}}$ so that the volume fraction and thermal stability of the TC phase are optimized.

Our neutron scattering experiment on $Ba_{0.2}Sr_{1.8}Co_2(Fe_{0.96}Al_{0.04})_{12}O_{22}$ also supports that the $\Delta E_{\text{barrier}}$ is enhanced by the Al substitution (Fig. S4) [25]. According to Fig. S4, the incommensurate $\boldsymbol{k} = (0, 0, \delta)$ peak, implying thermal repopulation of the ALC phase after the FC process, starts to dominantly appear above ∼200 K. On the other hand, in a previous neutron scattering study on the Al-free specimen $Ba_{0.3}Sr_{1.7}Co_2Fe_{12}O_{22}$, an incommensurate $\boldsymbol{k} = (0, 0, \delta)$ peak appeared above ∼120 K after the FC process [15]. This observation indicates that the specimen with $y = 0.04$ has a higher $\Delta E_{\text{barrier}}$ between the TC and the ALC phase. We note that a direct proof of the ALC phase in $Ba_{0.2}Sr_{1.8}Co_2(Fe_{0.96}Al_{0.04})_{12}O_{22}$ requires the observation of (1 0 L) peaks by a neutron diffraction study in future. However, based on the experimental evidence, i.e., observation of the c-axis polarization in $Ba_{0.2}Sr_{1.8}Co_2(Fe_{0.96}Al_{0.04})_{12}O_{22}$ (Fig. S5), systematic evolution of similar electrical phase boundaries in $Ba_{0.2}Sr_{1.8}Co_2(Fe_{1-y}Al_y)_{12}O_{22}$ ($y = 0.00$–0.04) (Fig. S6), and observation of a finite, significant slope in the low field M-H curve at 300 K (Fig. S7, 8), we herein argue that the ALC phase persistently exists in $Ba_{0.2}Sr_{1.8}Co_2(Fe_{1-y}Al_y)_{12}O_{22}$ ($y = 0.00$–0.06) at a broad temperature window at zero field bias [25].

IV. QUANTITATIVE COMPARISON OF THE ME EFFECTS IN $Ba_{2-x}Sr_xCo_2(Fe_{1-y}Al_y)_{12}O_{22}$

To understand how the phase competition and the thermal/magnetic stability of the TC phase can affect the electrical properties, we quantitatively compared the ME effects in the $Ba_{2-x}Sr_xCo_2Fe_{12}O_{22}$ series. First, Fig. 2(a) clearly shows that as x is increased, a sudden increase of P occurs at 10 K with a small H bias, and P almost reaches a maximum at $x = 1.6$–1.8. Moreover, the $x = 1.8$ compound still exhibits the most asymmetric P–H line shape, even at 200 K. Thus, to quantify the ME coupling strength, we defined ΔP_{Max} and $(dP/dH)_{\text{Max}}$ as follows: ΔP_{Max} represents the difference between the extrema of H-induced P, i.e., $P_{\text{Max}} - P_{\text{Min}}$, and $(dP/dH)_{\text{Max}}$ represents the maximum of dP/dH at a finite field near zero.

Based on the two quantities, we find that the sample with $x = 1.8$ in the $Ba_{2-x}Sr_xCo_2Fe_{12}O_{22}$ series exhibits the strongest ME coupling at all temperatures up to 250 K [Fig. 2(b)]. Although ΔP_{Max} is quite similar for both $x = 1.6$ and 1.8 below 200 K, ΔP_{Max} at 250 K is maximized at $x = 1.8$. Moreover, $(dP/dH)_{\text{Max}}$ up to 250 K is also maximized at $x = 1.8$. The enhancement of ΔP_{Max} and $(dP/dH)_{\text{Max}}$ in the $x = 1.8$ compound is closely related to the most asymmetric P–H line shape maintained up to a high temperature of 200 K,

indicating that the field-induced stabilization of the TC phase is linked to the enhancement. At a Sr ratio of $x = 1.8$, the variation of the three O-Fe-O bonding angles at the interface between the magnetic L and S blocks [Fig. 1(b)] and the resultant spin frustration among the three superexchange interactions are likely enhanced [29,34], initially leading to the ALC phase at zero field. Simultaneously, the $x = 1.8$ compound should also have a TC phase with enhanced field-induced metastability after the FC process as compared with the other compounds in the series, which can explain the maximized ΔP_{Max} and $(dP/dH)_{\text{Max}}$. Although a larger Sr concentration x may further optimize the spin frustration to increase the stability of the ALC phase at zero field and the field-induced metastability of the TC phase, we could not obtain high-quality single crystals with $x > 1.8$ because of the presence of large amounts of Fe_2O_3 and M-type hexaferrite impurities. Therefore, we have chosen $x = 1.8$ to investigate the effects of Al substitution to determine whether the ME properties can be further optimized.

As Al is substituted to form $Ba_{0.2}Sr_{1.8}Co_2(Fe_{1-y}Al_y)_{12}O_{22}$, we find that the P induced by a small H bias suddenly increases, resulting in an even sharper increase of ΔP_{Max} and $(dP/dH)_{\text{Max}}$ at all temperatures investigated. In particular, the compounds with $y = 0.02$–0.04 exhibit higher ΔP_{Max} and $(dP/dH)_{\text{Max}}$ than $Ba_{0.2}Sr_{1.8}Co_2Fe_{12}O_{22}$. On the other hand, as Al is increased further to, e.g., $y = 0.06$–0.08, the reversed amount of P by H tends to be suppressed even at 200 K so that the P–H curves become more symmetric. For example, the P–H curve becomes almost symmetric in the $y = 0.06$ compound at 200 K (Fig. S9) [25]. Our findings indicate that at a low Al doping level of $y = 0.00$–0.04, the Al substitution induces enhancement of the ME coupling via the increase of the metastable TC phase after the FC process. Furthermore, at a higher Al doping range of $y = 0.06$–0.08 and at high temperatures above 200 K, the sign change of P with H direction reversal is slowly suppressed, presumably owing to a decrease in the volume fraction of the field-induced TC phase. Consequently, the optimal volume fraction and thermal stability of the field-induced TC phase seem to be realized in the $y = 0.04$ specimen. We find that both ΔP_{Max} and $(dP/dH)_{\text{Max}}$ are maximized at $y = 0.04$ at 10 and 300 K, as summarized in Fig. 2(c). ΔP_{Max} is optimized to $430 \, \mu C/m^2$ at 10 K and $37 \, \mu C/m^2$ at 300 K, while $(dP/dH)_{\text{Max}}$ is ∼25 000 ps/m at 10 K and ∼1000 ps/m at 300 K.

V. FINE CONTROL OF MAGNETIC ANISOTROPY WITH Co AND Al SUBSTITUTION

In $Ba_{0.5}Sr_{1.5}Zn_2(Fe_{1-y}Al_y)_{12}O_{22}$, it is known that nonmagnetic Al^{3+} ions prefer to occupy the octahedral sites [6,35]. Consequently, the in-plane orbital angular momentum L_{ab} of the Fe^{3+} ions decreases, particularly in the off-centered octahedral site. This decrease in L_{ab} with Al substitution leads to weakened in-plane magnetic anisotropy, which in turn results in the change of spin structure from a proper screw type with only an in-plane spin component to a longitudinal conical spin structure with a c axis spin component. In the case of $Ba_{0.2}Sr_{1.8}Co_2Fe_{12}O_{22}$, Co $L_{2,3}$ edge x-ray absorption spectroscopy reveals that the Co^{2+} ions prefer to occupy the octahedral sites. Magnetic circular dichroism
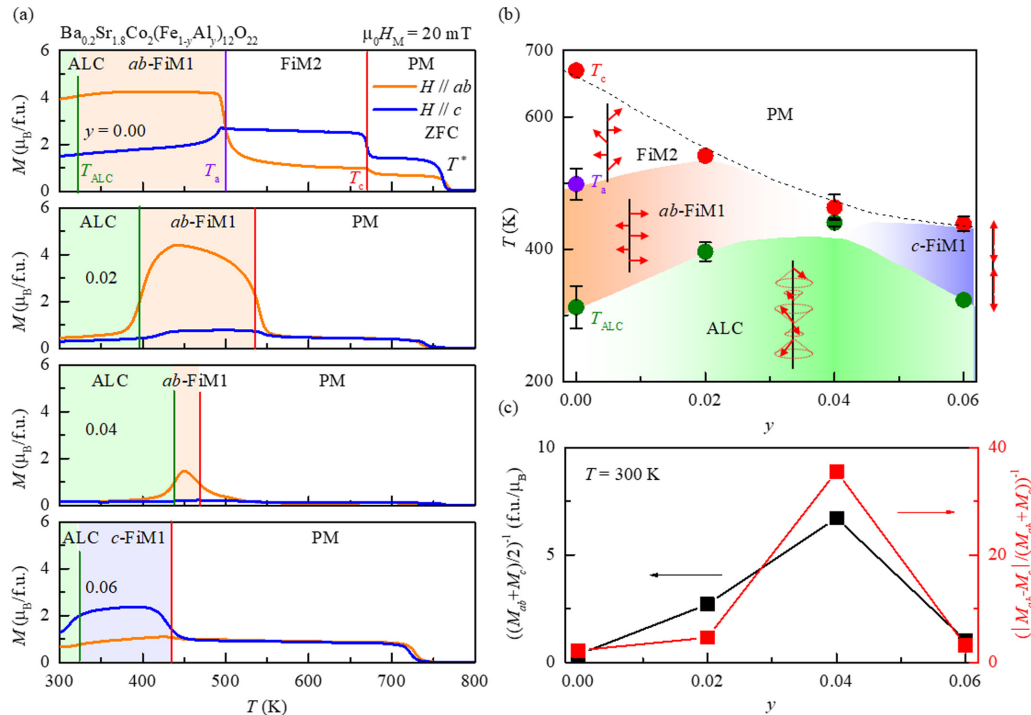
FIG. 4. (a) Magnetization curves along the *ab* (orange) and *c* (blue) direction measured under the application of $\mu_0 H_M = 20$ mT during the warming process after ZFC. Magnetic phases are divided into 5: ALC, *ab*-FiM1 (ferrimagnetic along the *ab* plane), *c*-FiM1 (ferrimagnetic along the *c* axis), FiM2 (canted ferrimagnetic tilted between the *ab* plane and *c* axis), and PM (paramagnetic). ALC, *ab*-FiM1, and *c*-FiM1 phases are highlighted by green, orange, and blue shadows, respectively. T_{ALC} (green solid line) denotes the transition temperature from ALC to the FiM1 phase. T_a indicates the temperature of the magnetic-anisotropy transition from the *ab*-plane to the tilted direction. T_c is the Curie temperature, showing a paramagnetic-to-ferrimagnetic transition. T^* indicates a local spin-ordering transition in the Fe-O-Fe bonds. (b) Magnetic phase diagram constructed from the magnetization curves in 4(a). The red arrows represent the spin structures in the phases. The long and short arrows indicate the spin in the *L* and *S* blocks, respectively. The ALC, *ab*-FiM1, and *c*-FiM1 phases are shown in green, red, and blue, respectively, to coincide with 4(a). The black dashed line indicates a trace of T_c drawn as a guide to the eye. (c) Plots of the inverse of $(M_{ab} + M_c)/2$ (left axis) and $|M_{ab} - M_c|/(M_{ab} + M_c)$ (right axis) against the Al doping ratio *y* at 300 K, demonstrating that the *y* = 0.04 specimen has the smallest average values of M_{ab} and M_c and the most isotropic magnetization curves.

measurements at the Fe and Co $L_{2,3}$ edges show that the substitution of Co^{2+} ions enhances the out-of-plane angular momentum L_c, forcing the spin moment toward the *c* axis [36]. As a result, the Co^{2+} ion not only stabilizes the ALC phase having a *c* axis spin component but also seems to intensify the superexchange interaction (possibly via the Co-O-Fe path) such that the transition temperature of the ALC phase, T_{ALC}, is above room temperature, in contrast to those of the corresponding Zn_2Y-type specimen. Therefore, $Ba_{0.2}Sr_{1.8}Co_2(Fe_{1-y}Al_y)_{12}O_{22}$ is expected to have not only a weakened L_{ab} due to the Al^{3+} substitution but also an increased L_c due to the Co^{2+} substitution. Accordingly, the Al^{3+} substitution in $Ba_{0.2}Sr_{1.8}Co_2(Fe_{1-y}Al_y)_{12}O_{22}$ enables us to achieve the fine control of magnetic anisotropy. Moreover, the Al substitution in one of the three octahedral Fe sites shown in Fig. 1(b) can change the degree of spin frustration and bond-angle variation at the interface. Such a delicate control of magnetic anisotropy as well as spin frustration could be crucial for stabilizing the ALC phase (at $H_{ab} = 0$) and TC phase (at $H_{ab} \neq 0$) to optimize the ME coupling near room temperature.

To find a clue on the interplay between *ab*-plane and *c*-axis magnetic anisotropy, we systematically investigated the temperature-dependent, in-plane magnetization (M_{ab}) and

out-of-plane magnetization (M_c) at a high temperature range (300 K < *T* < 800 K) after the ZFC process [Fig. 4(a)]. In the Al-free specimen $Ba_{0.2}Sr_{1.8}Co_2Fe_{12}O_{22}$, both M_{ab} and M_c exhibit a steplike increase at $T^* = 750$ K. Other specimens with Al substitution also exhibit a similar steplike increase in the magnetization curve at a proximately close T^* located within 750 K ± 30 K [37,38]. As this transition at T^* is nearly independent of the Al doping ratio and no appreciable impurity phase is observed in our single crystals, the transition is likely related to the local spin ordering arising from one of the Fe-O-Fe superexchange paths. Specifically, we suggest that the superexchange interaction between the Fe^{3+} in the tetrahedral sites and neighboring Fe^{2+} or Fe^{3+} ions in the octahedral sites plays a role to produce a local ferrimagnetic spin ordering, as similarly observed in other iron oxides, e.g., in magnetite at 850 K [39]. The relevant ferrimagnetic spin ordering between the effective magnetic *L* and *S* blocks in $Ba_{0.2}Sr_{1.8}Co_2Fe_{12}O_{22}$ is thus attributed to the steplike feature observed at $T_c = 670$ K [Fig. 4(a)]. (Note that for $Ba_2Co_2Fe_{12}O_{22}$, a similar transition has been identified at $T_c = 613$ K [28]). We find that T_c in $Ba_{0.2}Sr_{1.8}Co_2(Fe_{1-y}Al_y)_{12}O_{22}$ is systematically reduced with the increase of *y*, as indicated by the red solid lines in Fig. 4(a); $T_c = 670$, 541, 463, and 438 K for *y* = 0.0, 0.02, 0.04, and 0.06, respectively. This is consistent with the

expectation that the spin dilution effect with Al substitution decreases T_c. The red solid symbols in the phase diagram in Fig. 4(b) show this trend.

Another notable feature below T_c is that the magnitudes of M_{ab} and M_c measured at a bias field of $\mu_0 H_M = 20$ mT vary with y or temperature; in the $y = 0.00$ specimen, $M_{ab} \approx 1.0 \, \mu_B/\text{f.u.}$ and $M_c \approx 2.5 \, \mu_B/\text{f.u.}$ immediately below T_c, while $M_{ab} \approx 4.0 \, \mu_B/\text{f.u.}$ and $M_c \approx 1.8 \, \mu_B/\text{f.u.}$ below $T = 495$ K. This observation indicates that just below T_c, the ferrimagnetic moment was initially tilted off the c axis with a considerable ab-plane component. Then, a magnetic anisotropy transition occurs at 495 K, which is defined as T_a, to let the ab plane become an easy plane. We thus assign the phase below $T_a = 498$ K as a ferrimagnetic phase with dominant alignment along the ab plane, denoted as ab-FiM1, and the phase above T_a as a tilted ferrimagnetic phase FiM2. In the $y = 0.02$ and 0.04 specimens, a similar ab-FiM1 phase with a dominant M_{ab} moment is realized immediately below T_c. Finally, in the $y = 0.06$ specimen, a ferrimagnetic phase with a dominant M_c component, defined as c-FiM1, is realized at $T_c = 438$ K.

VI. MAGNETIC PHASE DIAGRAM REVEALING THE OPTIMAL STABILIZATION OF THE ALC PHASE

As shown in the magnetic phase diagram in Fig. 4(b), the ALC phase is located in a region where ferrimagnetic order with a net moment exhibits a crossover from an easy plane type (ab-FiM1) to an easy axis type (c-FiM1). When the ALC phase is formed at the transition temperature of T_{ALC} with decrease of temperature, both M_{ab} and M_c decrease at T_{ALC} [the green solid lines in Fig. 4(a)]. The T_{ALC} value for each y can be then extracted from the extrema in the curve of the temperature derivative of magnetization. Thus obtained $T_{ALC} = 312$ K for the $y = 0.00$ is consistent with a previous neutron diffraction study [15]. We find that at $y = 0.04$, T_{ALC} attains the highest value of 440 K. From an independent neutron diffraction study (Fig. S4) [25], we also confirmed the existence of the ALC phase at 380 K in the $y = 0.04$ compound. As summarized in the phase diagram of Fig. 4(b) (green solid circles), the evolution of T_{ALC} as a function of y thus forms a dome shape with an optimal $T_{ALC} = 440$ K at $y = 0.04$. This finding clearly proves that T_{ALC} is the highest around a doping level of $y = 0.04$.

The doping level of $y = 0.04$ seems to optimize not only the transition temperature but also the volume fraction of the ALC phase in competition with the ab-FiM1 or c-FiM1 phase. At $T = 300$ K, where the ALC phase is formed in all the specimens with different values of y, it is noticed that M_{ab} and M_c curves show two interesting features; the overall magnitudes of in-plane and out-of-plane magnetic moment $(M_{ab} + M_c)/2$, as well as the normalized difference between in-plane and out-of-plane magnetic moment, $|M_{ab} - M_c|/(M_{ab} + M_c)$, are minimized at $y = 0.04$. The inverse of $(M_{ab} + M_c)/2$ and $|M_{ab} - M_c|/(M_{ab} + M_c)$, plotted in Fig. 4(c), demonstrates these characteristic features in the magnetization curves. Because the ALC phase has effectively staggered the antiferromagnetic spin arrangement along the c axis, it is characterized by very low and isotropic magnetic moments. The behavior observed in Fig. 4(c) directly

shows that the volume fraction of the ALC phase is the highest in the $y = 0.04$ specimen at 300 K. The ALC phase with possibly staggered moment along the c axis closely competes with the ab-FiM1 and c-FiM1 phases formed at higher temperatures. Note that the results of Fig. 4(c) are still valid even if the net magnetic moment occurring due to local spin ordering below T^* is subtracted; Fig. S10 represents $(M_{ab} + M_c)/2$ and $|M_{ab} - M_c|/(M_{ab} + M_c)$ after correcting the magnetic moment at T^*, which shows a similar trend with Fig. 4(c) [25]. This observation again supports that the $y = 0.04$ compound still has the lowest magnetic moment among the $Ba_{0.2}Sr_{1.8}Co_2(Fe_{1-y}Al_y)_{12}O_{22}$ family regardless of the transition at T^*.

Combined with the evolution of M-T curves below $T = 300$ K, as presented in Fig. 3(a) and 3(b), the observation in the phase diagram of Fig. 4(b) indicates that the most stable doping of $y = 0.04$ for the ALC phase, which is formed after the ZFC process, coincides with the most stable TC phase, which is formed after the FC process along the ab plane. It is expected that the ALC phase would prefer the spin anisotropy along the c axis as compared with the TC phase because it has no net moment due to its staggered nature along the c axis (possibly with up (L)-up (S)-down (L)-down (S) configuration) (Note that the ab-plane moment also rotates in the plane to nearly cancel each other with an incommensurate propagation vector). The preferred c-axis spin anisotropy in the staggered antiferromagnetic ALC phase could be one key reason why the TC and ALC phases compete with each other thermodynamically and why H_{ab} and thermal fluctuations choose one phase over the other. In other words, the highest $\Delta E_{\text{barrier}}$ between the TC and ALC phases in Fig. 3(c) is achieved when the ALC phase is thermally most stable, possibly via the highest c axis spin anisotropy. Therefore, although the TC and ALC phase apparently look similar to each other in terms of their conical spin ordering patterns, they are clearly distinct each other in their spin anisotropy and in their net spin moment. It is thus inferred that $\Delta E_{\text{barrier}}$ is dependent on the differences in the spin anisotropy and the net magnetic moment of each magnetic phase, which in turn controls the metastable nature of each competing phase.

We emphasize that our findings here cannot be simply explained by a conventional view that the longitudinal conical phase is a favorable precursor phase to reach the TC phase. According to the earlier findings in the Mg_2Y hexaferrite $Ba_2Mg_2Fe_{12}O_{22}$, the TC phase is easily formed by the ab-plane magnetic field when the NLC phase with a finite spin moment along the c axis is formed thermally or a slanted conical phase is stabilized by application of H_{ab} [27]. In this case, the NLC or slanted conical phase seems to be continuously turned into the TC phase with the help of H_{ab}. Therefore, the NLC phase is likely recovered upon H_{ab} being reduced to become zero without exhibiting the metastable nature of the TC phase. As a result, the free energy landscape of the NLC phase is likely distinct from that of the ALC phase because the NLC phase, once realized, can be very close to the TC phase with a small $\Delta E_{\text{barrier}}$; both TC phase and NLC phase has a finite net moment that can rotate softly under magnetic fields while the ALC phase has no net moment and prefers the c-axis spin anisotropy, judging from the dominant staggered moment direction.

Our work clearly demonstrates that through systematic doping studies, the ALC phase without a net spin moment competes with the TC phase. Furthermore, the metastable nature of the TC phase realized by the *ab*-plane field becomes most conspicuous when the ALC phase preferring the *c*-axis spin anisotropy and staggering at zero magnetic field becomes most stable, which could be understood by the presence of the large energy barrier between the two phases. We thus provide an unprecedented understanding that *the thermal stability of the competing ALC phase is key to reaching the most metastable TC phase and, thereby, optimized ME coupling*. Furthermore, we show that the fine control of magnetic anisotropy via site-selective chemical substitution, e.g., Al^{3+} $y = 0.04$ doping in this case, is useful to make the ALC phase thermally most stable at zero field. It is likely that the degree of spin frustration at the interface is also controlled by the Al^{3+} substitution and also by the application of H_{ab} to eventually result in the highest volume fraction of the metastable TC phase and thus the highest ME coupling in the series of $Ba_{0.2}Sr_{1.8}Co_2(Fe_{1-y}Al_y)_{12}O_{22}$ specimen.

VII. CONCLUSION

We synthesized $Ba_{2-x}Sr_xCo_2(Fe_{1-y}Al_y)_{12}O_{22}$ ($1.0 \leqslant x \leqslant 1.8$ and $0.00 \leqslant y \leqslant 0.08$) single crystals to maximize the ME coupling strength by controlling the magnetic anisotropy and spin frustration. Systematic studies of the ME effects revealed that $Ba_{0.2}Sr_{1.8}Co_2(Fe_{0.96}Al_{0.04})_{12}O_{22}$ exhibits the highest magnetic-field-induced polarization and ME susceptibility dP/dH among the series of Co_2Y-type hexaferrites. The magnetization measurements after various ZFC and FC processes showed that the metastable TC and ALC phases coexist in all $Ba_{0.2}Sr_{1.8}Co_2(Fe_{1-y}Al_y)_{12}O_{22}$ compounds, indicating that the TC phase is separated from the ALC phase by the free-energy barrier at low temperatures. The evolution of M_{ab} after the FC and the neutron scattering results support that the free-energy barrier is modulated by Al substitution and is maximized in the $y = 0.04$ sample, i.e., $Ba_{0.2}Sr_{1.8}Co_2(Fe_{0.96}Al_{0.04})_{12}O_{22}$, making the TC phase thermally most stable. Furthermore, high-temperature studies of M_{ab} and M_c demonstrated that the cosubstitution of Co^{2+} and Al^{3+} ions allows the sensitive modulation of the magnetic anisotropy. Thus, T_{ALC} is maximized in the region of the phase diagram where *ab*-FiM1 and *c*-FiM1 compete with each other. Our observation shows that the stability of the ALC phase, as represented by the no net magnetization, is key to obtaining the optimized ME effect in the $y = 0.04$ sample. Finally, our strategy to achieve the optimized ME coupling in the series of Co_2Y-type hexaferrites is likely applicable to other hexaferrites with different transition-metal ions or different crystal structures.

VIII. METHODS

Single-crystalline $Ba_{2-x}Sr_xCo_2(Fe_{1-y}Al_y)_{12}O_{22}$ samples were grown via the Na_2O–Fe_2O_3 flux method with several thermal cycles in a platinum crucible. Electron probe microanalyses confirmed that the actual chemical compositions of our single crystals are close to the target nominal chemical formula of the flux growth process.

X-ray diffraction measurements were performed using a high-resolution x-ray diffractometer (Empyrean^{TM}, PANalytical). Grown single crystals were annealed in an oxygen atmosphere under pressure (5 MPa) at 800 C° to make them insulating enough to reduce leakage currents. For measuring the dielectric constant and the ME current along the *ab* plane, the hexagonal crystals were cut perpendicular to the *c* plane to form a flat surface with one side parallel to the *c* axis. Both wide surfaces of the sample were covered with a silver epoxy to form electrodes, and two copper wires were attached to them. Dielectric constants and ME currents were measured using a capacitance bridge (Andeen-Hagerling 2550 A) and an electrometer (Keithley 617), respectively.

To pole the sample before performing the ME current measurements, the maximum allowed electric-field bias without electrical breakdown (e.g., $\sim$3.0 MV/m at 10 K and $\sim$2.5 MV/m at 100 K) was applied along the [120] direction in the paraelectric collinear state ($\mu_0H = 5$ T) (see Fig. S11 for detailed poling electric fields) [25]. Subsequently, the electric field was turned off after H was reduced to achieve a ferroelectric state ($\mu_0H = 0.1$ T). The temperature and magnetic field were then controlled via a Physical Property Measurement System (PPMS^{TM}, Quantum Design) [40] to measure the ME or pyroelectric current. Finally, all magnetization data were acquired using a vibrating sample magnetometer equipped in the PPMS at both low temperatures below 300 K and high temperatures between 300 and 800 K. Neutron scattering results were obtained on the BT-4 triple axis spectrometer at the NIST Center for Neutron Scattering, an instrument collimation of 40.

[1] D. I. Khomskii, J. Magn. Magn. Mater. **306**, 1 (2006).

[2] D. V. Efremov, J. van den Brink, and D. I. Khomskii, Nat. Mater. **3**, 853 (2004).

[3] N. Hur, S. Park, P. A. Sharma, J. S. Ahn, S. Guha, and S.-W. Cheong, Nature (London) **429**, 392 (2004).

[4] I. Kagomiya, S. Matsumoto, K. Kohn, Y. Fukuda, T. Shoubu, H. Kimura, Y. Noda, and N. Ikeda, Ferroelectrics **286**, 167 (2003).

[5] R. Ramesh and N. A. Spaldin, Nat. Mater. **6**, 21 (2007).

[6] S. H. Chun, Y. S. Chai, Y. S. Oh, D. Jaiswal-Nagar, S. Y. Haam, I. Kim, B. Lee, D. H. Nam, K. T. Ko, J. H. Park, J. H. Chung, and K. H. Kim, Phys. Rev. Lett. **104**, 037204 (2010).

[7] S.-W. Cheong and M. Mostovoy, Nat. Mater. **6**, 13 (2007).

[8] A. Iyama and T. Kimura, Phys. Rev. B **87**, 180408(R) (2013).

[9] M. Tokunaga, M. Azuma, and Y. Shimakawa, J. Phys. Soc. Jpn. **79**, 064713 (2010).

[10] T. Kimura, Annu. Rev. Condens. Matter Phys. **3**, 93 (2012).

[11] Y. S. Chai, S. Kwon, S. H. Chun, I. Kim, B. G. Jeon, K. H. Kim, and S. Lee, Nat. Commun. **5**, 4208 (2014).

[12] S. H. Chun, Y. S. Chai, B.-G. Jeon, H. J. Kim, Y. S. Oh, I. Kim, H. Kim, B. J. Jeon, S. Y. Haam, J. Y. Park, S. H. Lee, J. H. Chung, J. H. Park, and K. H. Kim, Phys. Rev. Lett. **108**, 177201 (2012).

[13] T. Kimura, G. Lawes, and A. P. Ramirez, Phys. Rev. Lett. **94**, 137201 (2005).

[14] S. Shen, Y. Chai, and Y. Sun, Sci. Rep. **5**, 8254 (2015).

[15] H. B. Lee, S. H. Chun, K. W. Shin, B. G. Jeon, Y. S. Chai, K. H. Kim, J. Schefer, H. Chang, S. N. Yun, T. Y. Joung, and J. H. Chung, Phys. Rev. B **86**, 094435 (2012).

[16] H. B. Lee, Y. S. Song, J. H. Chung, S. H. Chun, Y. S. Chai, K. H. Kim, M. Reehuis, K. Proke, and S. Mat'A, Phys. Rev. B **83**, 144425 (2011).

[17] N. Momozawa, Y. Yamaguchi, and M. Mita, J. Phys. Soc. Jpn. **55**, 1350 (1986).

[18] T. Nakajima, Y. Tokunaga, M. Matsuda, S. Dissanayake, J. Fernandez-Baca, K. Kakurai, Y. Taguchi, Y. Tokura, and T. H. Arima, Phys. Rev. B **94**, 195154 (2016).

[19] H. Sagayama, K. Taniguchi, N. Abe, T. H. Arima, Y. Nishikawa, S. I. Yano, Y. Kousaka, J. Akimitsu, M. Matsuura, and K. Hirota, Phys. Rev. B **80**, 180419(R) (2009).

[20] Y. S. Chai, S. H. Chun, S. Y. Haam, Y. S. Oh, I. Kim, and K. H. Kim, New J. Phys. **11**, 073030 (2009).

[21] K. Taniguchi, N. Abe, S. Ohtani, H. Umetsu, and T.-H. Arima, Appl. Phys. Express **1**, 031301 (2008).

[22] V. Kocsis, T. Nakajima, M. Matsuda, A. Kikkawa, Y. Kaneko, J. Takashima, K. Kakurai, T. Arima, F. Kagawa, Y. Tokunaga, Y. Tokura, and Y. Taguchi, Nat. Commun. **10**, 1247 (2019).

[23] S. Shen, L. Yan, Y. Chai, J. Cong, and Y. Sun, Appl. Phys. Lett. **104**, 032905 (2014).

[24] S. Hirose, K. Haruki, A. Ando, and T. Kimura, Appl. Phys. Lett. **104**, 022907 (2014).

[25] See Supplemental Material at http://link.aps.org/supplemental/10.1103/PhysRevMaterials.5.034412 for details on the X-ray diffraction, neutron diffraction, magnetization, electric polarization, dielectric constant, and phase diagram.

[26] F. Wang, T. Zou, L. Q. Yan, Y. Liu, and Y. Sun, Appl. Phys. Lett. **100**, 122901 (2012).

[27] S. Ishiwata, Y. Taguchi, H. Murakawa, Y. Onose, and Y. Tokura, Science **319**, 1643 (2008).

[28] R. C. Pullar, Prog. Mater. Sci. **57**, 1191 (2012).

[29] N. Momozawa and Y. Yamaguchi, J. Phys. Soc. Jpn. **62**, 1292 (1993).

[30] S. Utsumi, D. Yoshiba, and N. Momozawa, J. Phys. Soc. Jpn. **76**, 034704 (2007).

[31] V. Kocsis, T. Nakajima, M. Matsuda, A. Kikkawa, Y. Kaneko, J. Takashima, K. Kakurai, T. Arima, Y. Tokunaga, Y. Tokura, and Y. Taguchi, Phys. Rev. B **101**, 075136 (2020).

[32] K. Zhai, Y. Wu, S. Shen, W. Tian, H. Cao, Y. Chai, B. C. Chakoumakos, D. Shang, L. Yan, F. Wang, and Y. Sun, Nat. Commun. **8**, 519 (2017).

[33] H. Ueda, Y. Tanaka, Y. Wakabayashi, and T. Kimura, Physica B **536**, 118 (2018).

[34] Y. Kitagawa, Y. Hiraoka, T. Honda, T. Ishikura, H. Nakamura, and T. Kimura, Nat. Mater. **9**, 797 (2010).

[35] W.-S. Noh, K. T. Ko, S. H. Chun, K. H. Kim, B. G. Park, J. Y. Kim, and J.-H. Park, Phys. Rev. Lett. **114**, 117603 (2015).

[36] W.-S. Noh *et al.* (unpublished).

[37] Y. Chang, K. Zhai, Y. Chai, D. Shang, and Y. Sun, J. Phys. D **51**, 264002 (2018).

[38] S. Hirose, K. Haruki, A. Ando, T. Kimura, and X. M. Chen, J. Am. Ceram. Soc. **98**, 2104 (2015).

[39] D. Levy, R. Giustetto, and A. Hoser, Phys. Chem. Miner. **39**, 169 (2011).

[40] NIST, Certain commercial equipment, instruments, or materials are identified in this paper to foster understanding. Such identification does not imply recommendation or endorsement by the National Institute of Standards and Technology, nor does it imply that the materials or equipment identified are necessarily the best available for the purpose.